Available online at www.sciencedirect.com
ScienceDirect
International Journal of Heat and Fluid Flow 28 (2007) 602–615
International Journal of HEAT AND FLUID FLOW
www.elsevier.com/locate/ijhff

# Near-wall, Reynolds-stress model calculations of transonic flow configurations relevant to aircraft aerodynamics

Suad Jakirlić [a,*], Bernhard Eisfeld [b], Roland Jester-zürker [a], Norbert Kroll [b]

[a] Chair of Fluid Mechanics and Aerodynamics, Department of Mechanical Engineering, Darmstadt University of Technology, Petersenstr. 30, D-64287 Darmstadt, Germany
[b] Institute of Aerodynamics and Flow Technology, DLR – German Aerospace Center, Lilienthalplatz 7, D-38108 Braunschweig, Germany

Received 4 December 2006; received in revised form 26 March 2007
Available online 15 May 2007

**Abstract**

The present work focuses on the application of two near-wall, wall-normal free, second-moment closure (SMC) models in the RANS (*Reynolds-Averaged Navier–Stokes*) framework in computing the (compressible) transonic flow past aircraft configurations and their elements (airfoils and wings). The flow geometries considered in this work include the transonic RAE 2822 profiles (cases 9 and 10), the ONERA M6 wing and the DLR-ALVAST wing-body configuration. The model results are analysed and discussed in conjunction with an available experimental database and the results of two widely used eddy-viscosity-based models, the one-equation Spalart–Allmaras model [Spalart, P.R., Allmaras, S.R., 1994. A one-equation turbulence model for aerodynamic flows. La Recherche Aérospatiale 1, 5–21] and the two-equation $k$–$\omega$ model of Wilcox [Wilcox, D.C., 1988. Reassessment of the scale-determining equation for advanced turbulence models. AIAA Journal 26, 1299–1310]. The SMC predictions show encouraging results with respect to the shock position, shock-affected flow structure and the strength of the wing-tip vortex.


*Keywords:* RANS; Reynolds-stress models; Eddy-viscosity models; Near-wall treatment; Transonic flow configurations; Aircraft aerodynamics

## 1. Introduction

Computational Fluid Dynamics (CFD) is nowadays regarded as an indispensable tool in aerodynamic design and optimization. The application of efficient CFD methods in aircraft aerodynamics and related disciplines enables reduction of costs and shortens substantially the time for development in aircraft industry. Furthermore, the employment of CFD methods supports to a large extent a detailed evaluation of new technologies and concepts as well as alternative configurations with respect to security, environmental (e.g., noise pollution) and economic aspects of transport and passenger aircrafts.

The turbulent, aerodynamic type flows with relevance to aircraft aerodynamics have been calculated in the past using almost exclusively simple, zero-equation turbulence models based on Prandtl's mixing length theory, such as Baldwin and Lomax (1978), Cebeci–Smith (1974) and Johnson–King (1985) models in the framework of the computational methods which solve the Navier–Stokes-type flow equations.[1] The latter model, known also as a half-equation model, solves in addition the ordinary differential equation governing the square root of the maximum shear stress component. While these turbulence models have been designed especially for the wing aerodynamics,

[1] Some inviscid computational methods based on solving the potential flow equations such as panel methods and methods computing the flowfield by solving the Euler equations accounting eventually for the viscous effects by interacting with a boundary-layer method are regarded as the most practical methods for engineering use. However, they are – although some appropriate extensions are proposed – to a large extent limited to the attached flows. The readers interested in more details about these methods are encouraged to consult the work of Cebeci (1999).

* Corresponding author. Tel.: +49 6151 163554; fax: +49 6151 164754.
*E-mail address:* s.jakirlic@sla.tu-darmstadt.de (S. Jakirlić).

0142-727X/$ - see front matter © 2007 Elsevier Inc. All rights reserved.
doi:10.1016/j.ijheatfluidflow.2007.04.001

increasing computer capacities, developments in grid generation and improved efficiency of numerical algorithms enable broader application of models based on the transport equations for turbulent quantities. Such model schemes include one-equation models, solving the equation governing the turbulent viscosity, e.g. Spalart–Allmaras model (SA, 1994), two-equation models based, for example on the scale-supplying variable $\omega$ denoting the inverse time scale of turbulence (Wilcox, 1988; Menter, 1994), or Reynolds-stress transport closures. The final report of the joint European project ECARP (European Computational Aerodynamic Research Project) on the validation of the CFD codes and assessment of turbulence models (Haase et al., 1997) offers a detailed insight into predictive capabilities of a broad range of turbulent models, especially transport models, in a large number of aerodynamic applications accounting for flow three-dimensionality, transonic configurations featuring shock-induced effects, separation, unsteady wakes, etc. Hereby, the contribution of Leschziner and Lien (1997) with respect to the use of full second-moment closure and non-linear eddy-viscosity transport models should be noted. Indeed, this project has been instrumental in introducing transport models into aerodynamic simulations for aircraft design in the industrial environment. Several other projects followed, for example the project MEGAFLOW within the framework of the German aerospace research program (Kroll et al., 2000) dealing with development and validation of efficient numerical tools for the aerodynamic calculation of complete aircraft in cruise, take-off and landing configurations. The recently completed FLOMANIA project – A European Initiative on Flow Physics Modelling – was almost entirely devoted to employment of sophisticated, mostly full (differential) Reynolds-stress models, Haase et al. (2006). The project is concluded with an application-oriented synthesis about the model's predictive performance on the basis of computing different aerodynamic flow configurations. A comprehensive survey article about the turbulence model assessment in aeronautics along with related numerical issues is given in the work of Leschziner and Drikakis (2002).

Together with the high-lift configurations corresponding to take-off and landing, the high-speed, cruise-flight configurations play an important role in the entire operational range of an aircraft. Transport and passenger aircrafts operate at cruise-flight velocities corresponding to a Mach number interval $Ma = 0.75$–$0.85$. The associated flow regime past an aircraft wing is of transonic nature. It is characterized by the development of a closed, wall-bounded supersonic flow region at the upper wing surface, Fig. 1 (its appearance on the lower wing surface is also possible depending on its curvature and the angle of attack). The flow is strongly accelerated, reaching sonic velocities at the leading edge of the wing. The supersonic region spreads behind the so-called sound line, denoting the isoline with $Ma = 1.0$. The pressure increase behind the maximum profile thickness causes the formation of a shock

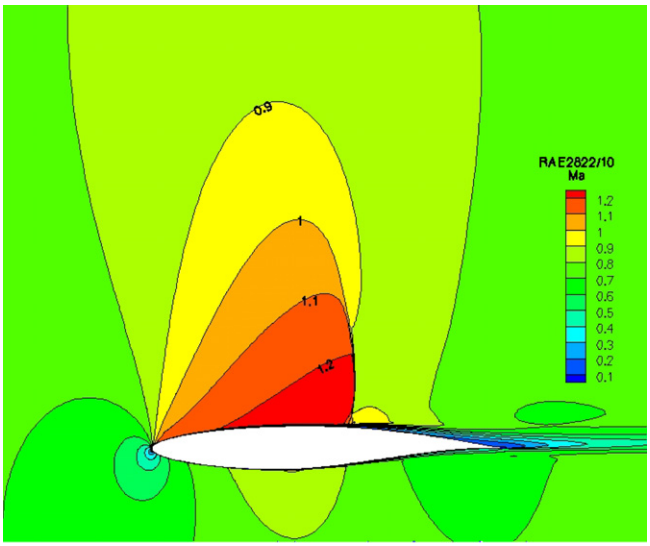


Fig. 1. Mach-number contours in the transonic flow around RAE2822 profile.

wave which closes the supersonic region. The shock front proceeds almost orthogonally to the wing profile contour. Transonic flows also exhibit boundary-layer/shock interaction, i.e. a boundary-layer thickening due to the adverse pressure gradient, and in some cases shock-induced separation occurs.[2] The change of the flow regime – from subsonic regime to supersonic and back – implies the solving of a combined elliptic/hyperbolic flow problem. These features as well as the compressible properties of the flow in general pose a special challenge not only for the numerical treatment but also for turbulence models. The present work focuses on the application of two near-wall second-moment closure (SMC) models, one accounting separately for both viscous effects and kinematic wall blockage with respect to the anisotropic nature of the Reynolds-stress and stress dissipation fields (Jakirlić and Hanjalić, 1995; Hanjalic and Jakirlic, 1998) and a second model, being a default Reynolds-stress transport model in the compressible flow solver DLR-FLOWer (Eisfeld et al., 2006).

Very extensive work on the computation of different shock-affected flow configurations, including also the RAE2822 airfoil, has been performed by Leschziner et al. (2000) and Batten et al. (1999). They applied several linear and non-linear, near-wall eddy-viscosity models and second-moment closure models, among others also the Jakirlić and Hanjalić (1995) model, whose updated version (see Section 2 for more details) is applied in the present work. The performance of the original linear HJ model was evaluated by computing the transonic flows over a plane channel bump (internal flow) and over an axisymmetric bump (both configurations are characterized by a strong pressure

[2] The transonic flow past aircraft wings can also exhibit unsteady shock/boundary-layer interaction caused by the shock position change due to self-excited oscillations. Readers interested in these, so-called transonic buffet flows are referred to the work of Barakos and Drikakis (2000).

increase in the supersonic portion of the flow, which is additionally enhanced by a much stronger cross-section constriction compared to the cases considered in the present work). These results were inferior to those obtained using the non-linear MCL (Modified Craft-Launder) model, especially with respect to the low intensity of the shock-induced flow reversal and pressure recovery. Batten et al. (1999) blamed the linear model of the redistribution term and conventional wall-reflection term due to Gibson and Launder (1978) used in the HJ model, the latter returning an excessive turbulence intensity in flows affected by strong deceleration (e.g. stagnation flow regions).

## 2. Computational method

The continuity, momentum and energy equations governing the compressible flow are given in differential form in the *Reynolds-Averaged Navier–Stokes* framework as follows:

$$\frac{\partial \bar{\rho}}{\partial t}+\frac{\partial}{\partial x_j}(\bar{\rho}\widetilde{U}_j)=0, \tag{1}$$

$$\frac{\partial(\bar{\rho}\widetilde{U}_i)}{\partial t}+\frac{\partial}{\partial x_k}(\bar{\rho}\widetilde{U}_i\widetilde{U}_k+\bar{\rho}\widetilde{u_i''u_k''})=-\frac{\partial \overline{P}}{\partial x_i}+\frac{\partial \bar{\tau}_{ik}}{\partial x_k}, \tag{2}$$

$$\frac{\partial(\bar{\rho}\widetilde{E})}{\partial t}+\frac{\partial}{\partial x_k}(\bar{\rho}\widetilde{H}\widetilde{U}_k+\bar{\rho}\widetilde{u_i''u_k''}\widetilde{U}_i)=\frac{\partial}{\partial x_k}(\bar{\tau}_{ik}\widetilde{U}_i)-\frac{\partial}{\partial x_k}(\bar{q}_k+\bar{q}_k^{(t)})+\bar{\rho}D_{kk} \tag{3}$$

with total energy $\widetilde{E}=\tilde{e}+\widetilde{U}_k\widetilde{U}_k/2+\tilde{k}(\tilde{e}=C_v\widetilde{T})$ and total enthalpy $\widetilde{H}=\tilde{h}+\widetilde{U}_k\widetilde{U}_k/2+\tilde{k}(\tilde{h}=C_p\widetilde{T})$. In these equations the overbar ($\bar{\phi}$) and the tilde ($\tilde{\phi}$) denote simple and mass weighted averages, respectively. Here, a Newtonian fluid with the stress tensor and a Fourier type heat flux

$$\bar{\tau}_{ij}=2\bar{\mu}\widetilde{S}_{ij};\tilde{S}_{ij}=\frac{1}{2}\left(\frac{\partial \widetilde{U}_i}{\partial x_j}+\frac{\partial \widetilde{U}_j}{\partial x_i}-\frac{2}{3}\frac{\partial \widetilde{U}_k}{\partial x_k}\delta_{ij}\right), \tag{4}$$

$$\bar{q}_i=-\bar{\lambda}\frac{\partial \widetilde{T}}{\partial x_i} \tag{5}$$

is assumed. In these material laws the dynamic viscosity follows from Sutherland's formula and the heat conductivity is related to the dynamic viscosity via a constant Prandtl number. Thermodynamic closure is achieved by the assumption of an ideal ($\overline{P}=\overline{\rho}\Re\widetilde{T}$), calorically perfect gas. Note, that the contribution of turbulent diffusion $\bar{\rho}D_{kk}(=\partial(\overline{\rho u_i''u_i''u_k''}/2-\overline{u_i''\tau_{ik}})b/\partial x_k)$ to the total energy Eq. (3) and the contributions of the kinetic energy of turbulence to the total energy $\widetilde{E}$ and total enthalpy $\widetilde{H}$ are usually neglected. This simplification was followed also in the present work.

The turbulent heat flux is modelled in analogy to Fourier type heat conduction

$$\bar{q}_i^{(t)}(=\overline{\rho h u_k''})=-\bar{\lambda}^{(t)}\frac{\partial \widetilde{T}}{\partial x_i}, \tag{5.1}$$

where the eddy conductivity is computed from an equivalent eddy-viscosity via the definition of the turbulent Prandtl number, i.e.

$$\bar{\lambda}^{(t)}=\frac{C_p\bar{\mu}^{(t)}}{Pr_t} \tag{5.2}$$

with $\bar{\mu}^{(t)}$ determined by an eddy-viscosity model scheme. The following sections outline the description of the turbulence models used and numerical method applied.

### 2.1. Turbulence modelling

The computations were performed with a wall-normal free version of the low-Re number Second-Moment (Reynolds-stress) closure model (RSM) due to Hanjalic and Jakirlic (HJ, 1998). The model satisfies all important requirements, with a specific emphasis on limiting states of turbulence (vanishing and very high turbulence *Re* numbers, two-component limit, etc.), reproducing the laminar-to-turbulent and reverse transition (by-pass and shear-generated transition with minimum background turbulence), appropriate reproduction of effects of extra strain rates (transverse shear, skew-induced three-dimensionality), high acceleration (including laminarization), high deceleration (approaching separation), swirl effects, mean compression, flow separation, recirculation and reattachment, see e.g. Hanjalić and Jakirlić (2002). The best illustration for the model's ability to account properly for a large deviation from the equilibrium conditions is given in Fig. 2, where semi-log plots of the mean velocity are presented for several boundary layer flows subjected to different pressure gradients (favourable and adverse) featuring the flow phenomena pertinent to aircraft aerodynamics.

Another interesting model feature accounts separately for the wall effects on anisotropy of stress bearing and dissipative scales by introducing both the turbulent stress and dissipation rate anisotropy ($A$ and $E$; $A=1–9(A_2-A_3)/8$, $A_2=a_{ij}a_{ji}$, $A_3=a_{ij}a_{jk}a_{ki}$; $E=1–9(E_2-E_3)/8$, $E_2=e_{ij}e_{ji}$,

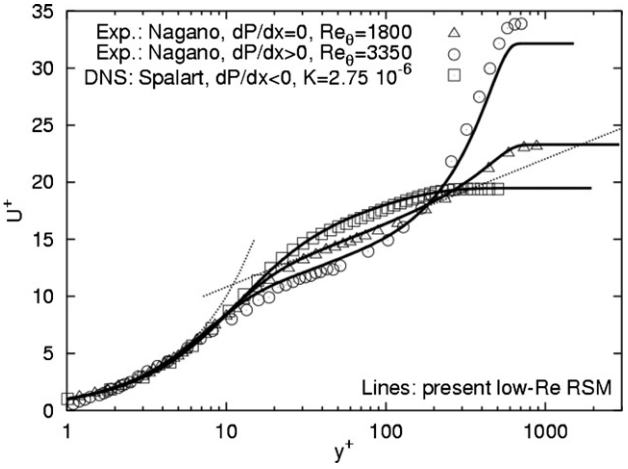


Fig. 2. Semi-log plots of the mean axial velocity in the boundary-layers subjected to different pressure gradients.

$E_3 = e_{ij}e_{jk}e_{ki}$), in addition to viscosity effects taken into account via $Re_t = \tilde{k}^2/(\nu\varepsilon)$. The strong difference in the anisotropy rates of both tensors ($a_{ij} = \widetilde{u_i''u_j''}/\tilde{k} - 2\delta_{ij}/3$ and $e_{ij} = \varepsilon_{ij}/\varepsilon - 2\delta_{ij}/3$) expressed in terms of their two-componentality factors $A$ and $E$ and the turbulence model capability to capture them correctly is shown in Fig. 3. Fig. 3 displays also the normal Reynolds-stress intensities across the zero-pressure gradient boundary-layer at the location corresponding to $Re_\theta = 1410$. It should be noted that this result is obtained by starting from the laminar flow in front of the flat plate and prescribing the location where an abrupt transition occurs (the source terms in the Reynolds-stress equation – production, redistribution and dissipation – are multiplied by a step-function taking zero value in the laminar region and unity value in the turbulent region). Even better agreement, especially concerning the streamwise stress component, is obtained when starting from turbulent input profiles (not shown here).

The precise specification of the entire turbulence model is given below. The present near-wall, second-moment closure model is based on the model equations governing the Reynolds-stress tensor and the dissipation rate of the kinetic energy of turbulence:

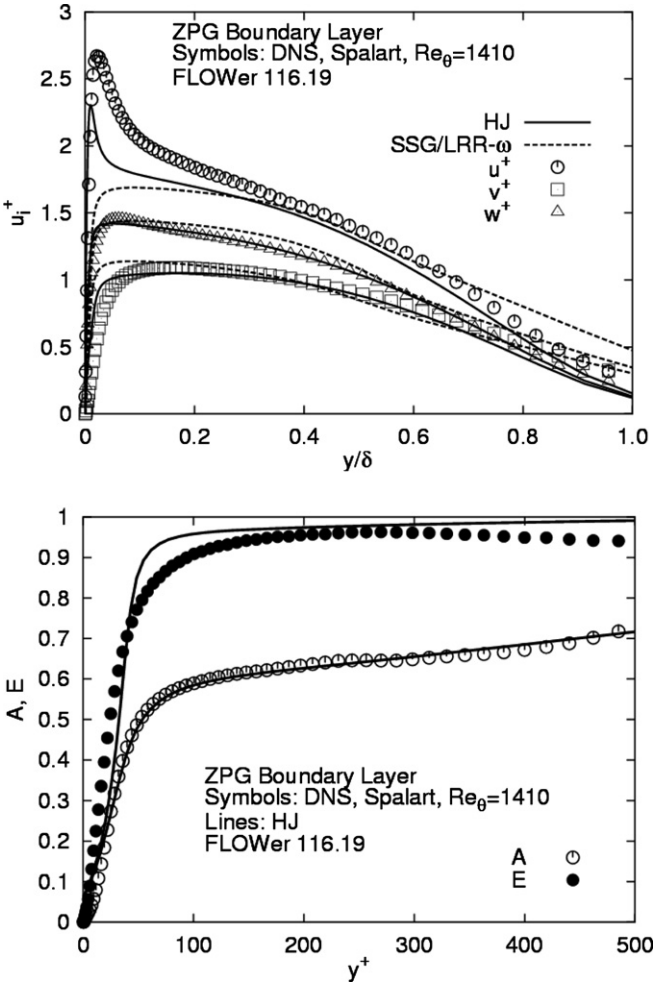


Fig. 3. Reynolds-stress components (upper) and two-componentality parameters $A$ and $E$ (lower) in a zero-pressure gradient boundary-layer.

$$\frac{\partial(\bar{\rho}\widetilde{u_i''u_j''})}{\partial t} + \frac{\partial(\bar{\rho}\widetilde{U}_k\widetilde{u_i''u_j''})}{\partial x_k} = \frac{\partial}{\partial x_k}\left[\left(\bar{\mu}\delta_{kl} + C_s\bar{\rho}\frac{\tilde{k}}{\varepsilon}\widetilde{u_k''u_l''}\right)\frac{\partial\widetilde{u_i''u_j''}}{\partial x_l}\right] + \bar{\rho}P_{ij} - \bar{\rho}\varepsilon_{ij} + \bar{\rho}\Phi_{ij} + \bar{\rho}\Phi_{ij}^w, \tag{6}$$

$$\frac{\partial(\bar{\rho}\varepsilon)}{\partial t} + \frac{\partial(\bar{\rho}\widetilde{U}_k\varepsilon)}{\partial x_k} = \frac{\partial}{\partial x_k}\left[\left(\bar{\mu}\delta_{kl} + C_\varepsilon\bar{\rho}\frac{\tilde{k}}{\varepsilon}\widetilde{u_k''u_l''}\right)\frac{\partial\varepsilon}{\partial x_l}\right] + \bar{\rho}(C_{\varepsilon,1}P_k - C_{\varepsilon,2}\varepsilon)\frac{\varepsilon}{\tilde{k}} + C_{\varepsilon,3}\bar{\mu}\frac{\tilde{k}}{\varepsilon}\widetilde{u_j''u_k''} \times \frac{\partial^2\widetilde{U}_i}{\partial x_j\partial x_l}\frac{\partial^2\widetilde{U}_i}{\partial x_k\partial x_l} \tag{7}$$

with stress production term $P_{ij} = -\widetilde{u_iu_k}\partial\widetilde{U}_j/\partial x_k - \widetilde{u_ju_k}\partial\widetilde{U}_i/\partial x_k$ and $P_k = -\widetilde{u_iu_j}\partial\widetilde{U}_i/\partial x_j$ being the production rate of the kinetic energy of turbulence. The coefficients $C_S$ and $C_\varepsilon$ take the values 0.22 and 0.18, respectively. The stress dissipation tensor was modelled by using the following anisotropic formulation

$$\varepsilon_{ij} = f_s\widetilde{u_i''u_j''}\frac{\tilde{k}}{\varepsilon} + (1 - f_s)\frac{2}{3}\varepsilon\delta_{ij} \tag{8}$$

with $f_s = 1 - \sqrt{A}E^2$ (one should note that this formulation doesn't result in the correct asymptotic behaviour of the $\varepsilon_{22}$, $\varepsilon_{12}$ and $\varepsilon_{23}$ components, but this fact caused only a slight near-wall imbalance in the equations governing the stress components comprising the normal-to-the-wall fluctuation and has marginal effect on other components) and a quadratic formulation of the pressure–strain model

$$\begin{aligned}
&\Phi_{ij} = \Phi_{ij,1} + \Phi_{ij,2},\\
&\Phi_{ij,1} = -\varepsilon\left[C_1a_{ij} - C_1'\left(a_{ik}a_{jk} - \frac{1}{3}A_2\delta_{ij}\right)\right],\\
&\Phi_{ij,2} = -C_2'a_{ij}P_k + C_3\tilde{k}\widetilde{S}_{ij} + C_4\tilde{k}(a_{ip}\widetilde{S}_{pj} + a_{jp}\widetilde{S}_{pi} - \frac{2}{3}a_{pq}\widetilde{S}_{pq}\delta_{ij}) - C_5\tilde{k}(a_{ip}\widetilde{W}_{jp} + a_{jp}\widetilde{W}_{ip})
\end{aligned} \tag{9}$$

with mean vorticity tensor $\widetilde{W}_{ij} = 0.5(\partial\widetilde{U}_i/\partial x_j - \partial\widetilde{U}_j/\partial x_i)$. The wall reflexion term model

$$\Phi_{ij}^w = C_1^w f_w\frac{\varepsilon}{\tilde{k}}\left(\widetilde{u_k''u_m''}n_kn_m\delta_{ij} - \frac{3}{2}\widetilde{u_i''u_k''}n_kn_j - \frac{3}{2}\widetilde{u_k''u_j''}n_kn_i\right) + C_2^w f_w\frac{\varepsilon}{\tilde{k}}\left(\Phi_{km,2}^{IP}n_kn_m\delta_{ij} - \frac{3}{2}\Phi_{ik,2}^{IP}n_kn_j - \frac{3}{2}\Phi_{kj,2}^{IP}n_kn_i\right), \tag{10}$$

$$\Phi_{ij,2}^{IP} = -C_2\left(P_{ij} - \frac{2}{3}P_k\delta_{ij}\right) \tag{11}$$

was made wall-normal free by introducing a unit vector pointing into the direction of the non-homogeneity of the turbulence field, in line with the proposal of Gerolymos and Vallet (2002): $n_i = \nabla(A\tilde{k}^{3/2}/\varepsilon)/|\nabla(A\tilde{k}^{3/2}/\varepsilon)|$. As indicated in Eq. (10), the linear, *isotropization-of-production* (IP, Launder et al., 1975) form of the rapid pressure–strain model (Eq. (11), with $C_2$ defined in Eq. (12)) was retained

in the term denoting the wall influence on the rapid pressure scrambling process.

The model coefficients and functions are summarized as follows:

$$C_1 = C + \sqrt{A}E^2; \quad C = 2.5AF^{1/4}f,$$
$$C_1' = \max[0.8A_2; 0.5]C_1,$$
$$C_2 = 0.6A^{1/2}; \quad C_3 = \frac{4}{3}C_2; \quad C_4 = C_2, \tag{12}$$
$$C_5 = C_2; \quad C_2' = 0; \quad F = \min[0.6; A_2],$$
$$f = \min\left[\left(\frac{Re_t}{150}\right)^{3/2}; 1\right],$$
$$C_1^w = \max[0.9 - 0.7C; 0.3],$$
$$C_2^w = \min[A; 0.3], \tag{13}$$
$$f_w = \min\left[\frac{k^{3/2}}{C_l \varepsilon y_n}; 1.4\right]; \quad C_l = 2.5,$$
$$C_{\varepsilon,1} = 1.44; \quad C_{\varepsilon,2} = 1.8; \quad C_{\varepsilon,3} = 0.3 \tag{14}$$

with $y_n$ representing the wall closest distance. The functional dependency of the coefficient $C_1'$ in the non-linear part of the slow term is obtained by a method for an *a priori* determination of the model coefficients, Jakirlić (2004). The $C_2'$ profiles obtained from the DNS database of the plane channel flow for $Re_\tau = 180$ (Moser et al., 1999) using the same method[3] exhibit values between −0.2 and 0.2, missing by far the positive value in, e.g., the Speziale, Speziale et al. (1991) – SSG model ($C_2' = 0.9$, Table 1), whereas the evaluated profiles of the coefficients $C_4$ and $C_5$ exhibit the values agreeing well with the SSG proposal. The appropriate value and even the sign of the coefficient $C_2'$ remain to be clarified. Because of this uncertainty its value was set to zero in the present work, i.e. the linear model for the rapid part was applied (Eqs. (12)–(14)).

The wall boundary condition is based on the asymptotic behaviour of the Taylor microscale $\lambda(\lambda = \sqrt{5}y + \cdots$, Fig. 4) and its exact relationship to the dissipation rate in the immediate wall vicinity: $\varepsilon = 10\nu\tilde{k}/\lambda^2$ (see Fig. 4 for comparison of the dissipation rate obtained by this formulation and the DNS database in all characteristics region of a backward-facing step flow). Its linear dependency on the wall distance through the entire viscous sublayer (even up to $y/H \approx 0.04$ – $H$ being the step height – corresponding to $y^+ \approx 10$ at $x/H = 19$, Fig. 4) enables the wall-closest grid node to be positioned immediately below the edge of the viscous sublayer, leading to a substantial coarsening of the near-wall grid resolution. The profiles of all quantities

[3] For each combination of three different components (e.g., $ij = 11$, $ij = 22$ and $ij = 12$; other combinations can also be used) of the rapid term, the model formulation for $\Phi_{ij,2}$ (Eq. (9)) can be written as a system of three equations with three unknowns $C_2'$, $C_4$ and $C_5$ ($C_3$ coefficient has been taken as known, e.g., $C_3 = 0.8 - 0.65\sqrt{A_2}$ in the SSG model, Table 1). The input data for all variables (also for $\Phi_{ij,2}$) were taken from the DNS database of a fully-developed channel flow.

Table 1
Closure coefficients for the LRR and SSG contributions to the SSG/LRR-$\omega$ pressure redistribution model (Eq. (9))

| | $C_1$ | $C_1'$ | $C_2'$ | $C_3$ | $C_4$ | $C_5$ |
|---|---|---|---|---|---|---|
| LRR | 1.8 | 0.0 | 0.0 | 0.8 | $(18C_2^{LRR}+12)/22$ | $(-14C_2^{LRR}+20)/22$ |
| SSG | 1.7 | 1.05 | 0.9 | $0.8–0.65\sqrt{A_2}$ | 0.625 | 0.2 |

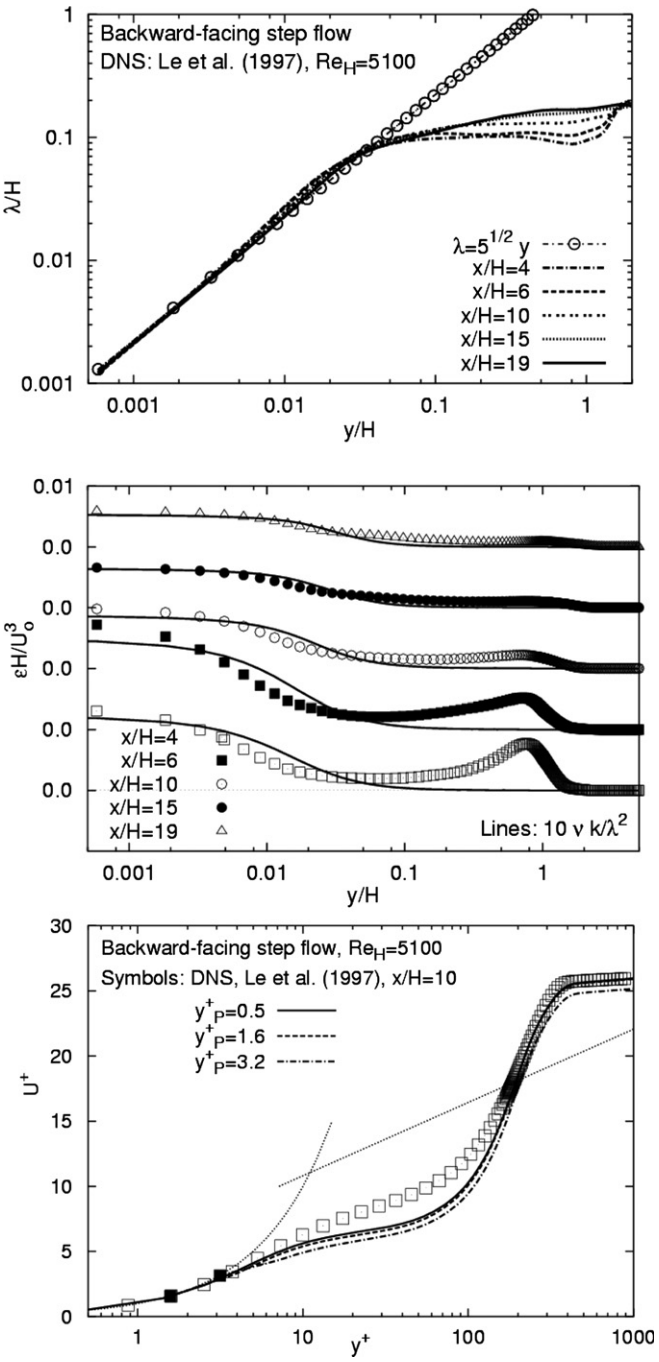


Fig. 4. Near-wall behaviour of Taylor microscale $\lambda$ (upper) and dissipation rate profiles at selected locations in the backward-facing step flow (middle) ($x/H = 4$ and 6 – recirculation zone, $x/H = 10$, 15 and 19 – recovery region) and semi-log profile of the mean axial velocity at $x/H = 10$ (lower). DNS (Le et al., 1997).

in the remainder of the cross-section follow closely the result obtained on the finest grid, as it is demonstrated on the semi-log profile of the mean axial velocity, Fig. 4. This approach provides bridging of a portion of the viscous sublayer, higher grid flexibility with respect to flow regions featured by different phenomena and weaker sensitivity against the grid non-uniformities in the near-wall regions.

The second near-wall, Reynolds-stress transport model used in the present work (denoted as SSG/LRR-$\omega$ throughout the manuscript) represents a default second-moment closure model in the compressible computer code DLR-FLOWer. This model scheme, proposed by Eisfeld et al. (2006), represents a numerically robust combination of the Launder–Reece–Rodi (LRR, 1975) model resolving the near-wall layer with the Speziale–Sarkar–Gatski (Speziale et al., 1991) model (with linear formulation of the slow part) being employed in the outer region. The coefficients in this hybrid model are weighted between the values used in the basic models by applying Menter's blending function $F_1$ (Menter, 1994). Menter's baseline $\omega$-equation ($\omega = \varepsilon/(C_\mu \tilde{k}), C_\mu = 0.09$) is exploited for supplying the length scale. It should be noted, that the coefficients in the LRR model arose from its $\omega$-based, near-wall adaptation proposed by Wilcox (1998). Hereby, the wall-reflection term was omitted.

All coefficients featured in the model of the redistribution term (Eq. (9)) are obtained from the following blending relationship:

$$C_i = F_1 C_i^{\mathrm{LRR}} + (1 - F_1) C_i^{\mathrm{SSG}}. \tag{15}$$

The respective coefficients of the SSG and LRR model fractions are listed in Table 1 with $C_2^{\mathrm{LRR}} = 0.5556$. The resulting value of the new coefficient in the model of turbulent diffusion (Eq. (6)) was obtained using the same blending procedure: $C_S' = F_1 \sigma^* + (1 - F_1) C_S$ with $\sigma^* = 0.5$. The Rotta's isotropic model was adopted for the dissipation correlation: $\varepsilon_{ij} = 2\varepsilon\delta_{ij}/3$ (i.e. $\varepsilon_{ij} = 2C_\mu \tilde{k}\omega\delta_{ij}/3$).

The model equation governing the specific time scale $\omega$ was formulated in line with the proposition due to Menter (1994):

$$\begin{aligned}\frac{\partial(\bar{\rho}\omega)}{\partial t} + \frac{\partial(\bar{\rho}\widetilde{U}_k\omega)}{\partial x_k} = {} & \frac{\partial}{\partial x_k}\left[\left(\bar{\mu} + \sigma_\omega \bar{\rho}\frac{\tilde{k}}{\omega}\right)\frac{\partial\omega}{\partial x_k}\right] \\ & - \alpha_\omega \bar{\rho}\frac{\omega}{\tilde{k}}\widetilde{u_i'' u_k''}\frac{\partial \widetilde{U}_i}{\partial x_k} - \beta_\omega \bar{\rho}\omega^2 \\ & + \sigma_d \frac{\bar{\rho}}{\omega}\left(\frac{\partial\omega}{\partial x_k}\frac{\partial\tilde{k}}{\partial x_k}; 0\right).\end{aligned} \tag{16}$$

Table 2
Closure coefficients for the LRR and SSG contributions to the $\omega$-equation (Eq. (16)) in the SSG/LRR-$\omega$ model

| | $\alpha_\omega$ | $\beta_\omega$ | $\sigma_\omega$ | $\sigma_d$ |
|---|---|---|---|---|
| LRR | 0.5556 | 0.075 | 0.5 | 0 |
| SSG | 0.44 | 0.0828 | 0.856 | $2\sigma_\omega^{\mathrm{SSG}}$ |

The final values of the model coefficients (see Table 2 for the individual coefficient values) were obtained by using the blending procedure formulated in Eq. (15). The blending function $F_1$ is defined after Menter, 1994) as

$$F_1 = \tanh(\varsigma^4) \tag{17}$$

with the argument $\zeta$ taking the following form:

$$\varsigma = \min\left[\max\left(\frac{\sqrt{\tilde{k}}}{C_\mu \omega d^2}; \frac{500\bar{\mu}}{\bar{\rho}\omega d^2}\right); \frac{4\sigma_\omega^{\mathrm{SSG}}\bar{\rho}\tilde{k}}{\bar{\rho}C_D^{\mathrm{SSG}}d^2}\right], \tag{18}$$

$$\bar{\rho}C_D^{\mathrm{SSG}} = \sigma_d^{\mathrm{SSG}}\frac{\bar{\rho}}{\omega}\max\left(\frac{\partial k}{\partial x_k}\frac{\partial\omega}{\partial x_k}; 0\right), \tag{19}$$

where $d$ (Eq. (18)) denotes the wall distance. Because of the constant values of the model coefficients in the pressure redistribution model (Eqs. (9) and (15), Table 1), its slow part does not vanish at the wall for all components. It means that the two-componentality parameter $A$ does not approach the zero value at the wall, reflecting the model's non-capability to fully resolve the stress anisotropy in the thin, immediate wall vicinity. Beyond this region, characterized by a strong peak of the streamwise stress component, the Reynolds-stress intensities display good agreement with the DNS results, Fig. 3 (upper). Despite this deviation the model is capable of correctly capturing the pressure redistribution in flows affected by shock/boundary-layer interaction and related phenomena, as it will be illustrated in Section 3.

In addition, all cases considered were computed by two popular eddy-viscosity-based models being extensively used for the aerodynamics applications: the Spalart–Allmaras eddy-viscosity transport model (1994) and the Wilcox's (1988) $k$–$\omega$ model.

### 2.2. Numerical method

All computations were performed by using the DLR FLOWer code, which is well established in the academic research and aeronautical industry. It employs a variety of turbulence models, ranging from eddy-viscosity models (Baldwin–Lomax, Spalart–Allmaras type, $k$–$\omega$ type) to full Reynolds-stress models (Wilcox stress-$\omega$, SSG/LRR-$\omega$), which have been validated in a large number of test cases, ranging from baseline to complete aircraft flow configurations, Kroll et al. (2002), Eisfeld et al. (2006), Eisfeld and Brodersen (2005). The DLR FLOWer code is a Finite Volume method for block-structured meshes, solving the afore-mentioned compressible RANS equations with any of the above turbulence models. For the RANS equations different spatial discretization schemes are available, where the most common one is a second-order central scheme with artificial dissipation.

The DLR-FLOWer code is density-based, solving the coupled system of conservation equations for mass, momentum, total energy and turbulent quantities in their time-dependent, integral formulation

$$\int\int\int_V \frac{\partial \vec{W}}{\partial t}\,\mathrm{d}V + \oint_S \int (\overline{\overline{F}}_c - \overline{\overline{F}}_v)\cdot\vec{n}\,\mathrm{d}S - \int\int\int_V \vec{Q}\,\mathrm{d}V = 0,$$

where $\partial\vec{W}/\partial t$ represents the time-derivative of the vector of conservation variables, $\overline{\overline{F}}_c$ and $\overline{\overline{F}}_v$ are the tensors of convective and viscous fluxes, respectively, and $\vec{Q}$ contains the source terms.

The FLOWer code uses a cell-centered Finite Volume discretization (Kroll et al., 1995), i.e. the above equation is solved for each individual mesh cell $i$ according to

$$\frac{\partial \vec{W}_i}{\partial t} = -\frac{1}{V_i}\left[\sum_j \left(\overline{\overline{F}}_c - \overline{\overline{F}}_v\right)^j \cdot \vec{S}^j - \vec{Q}\right]_i,$$

where $V_i$ is the volume of the cell and $\vec{S}^j$ its $j$ surface vectors, which are assumed constant on each face.

Let the index $i+1/2$ denote the face between cells $i$ and $i+1$. Then, using a central space discretization, the convective fluxes over a face are taken as the arithmetic average of the corresponding flux functions in the adjacent cells, i.e.

$$(\overline{\overline{F}}_c)^{i+1/2} = \overline{\overline{F}}_c(\vec{W}^{i+1/2}),$$

where

$$\vec{W}^{i+1/2} = \frac{1}{2}(\vec{W}^i + \vec{W}^{i+1}).$$

However, such a central scheme is unstable and requires an artificial dissipation term, so that the above equation has to be modified to

$$\frac{\partial \vec{W}_i}{\partial t} = -\frac{1}{V_i}\left\{\sum_j \left[(\overline{\overline{F}}_c)^j \cdot \vec{S}^j - \sigma^j \vec{D}^j\right] - \sum_j \left[(\overline{\overline{F}}_v)^j \cdot \vec{S}^j\right] - Q\right\}_i,$$

where the corresponding artificial dissipation flux is given according to Jameson et al. (1981) by

$$\vec{D}^{i+1/2} = \alpha^{i+1/2}\Big[(\varepsilon^{(2)})^{i+1/2}(\vec{W}_{i+1} - \vec{W}_i) - (\varepsilon^{(4)})^{i+1/2}(\vec{W}_{i+2} - 3\vec{W}_{i+1} + 3\vec{W}_i - \vec{W}_{i-1})\Big]$$

and its sign is defined by

$$\sigma^{i+1/2} = -\sigma^{i-1/2} = 1.$$

The coefficients

$$(\varepsilon^{(2)})^{i+1/2} = k^{(2)}\max(\upsilon_{i+2}, \upsilon_{i+1}, \upsilon_i, \upsilon_{i-1}),$$
$$(\varepsilon^{(4)})^{i+1/2} = \max[0, k^{(4)} - (\varepsilon^{(2)})^{i+1/2}]$$

with the indicator for pressure gradients

$$\upsilon = \frac{|p_{i+1} - 2p_i + p_{i-1}|}{|p_{i+1} + 2p_i + p_{i-1}|},$$

where $p$ is the pressure, are constructed in such a way, that the scheme is automatically switching to first-order accuracy at shocks. This avoids oscillations of the solution. The coefficients $k^{(2)}$ and $k^{(4)}$ define the level of artificial dissipation close to the shock and in the regions, where the solution is smooth, respectively. Typical values are $k^{(2)} = 1/2$ and $k^{(4)} = 1/64$.

The coefficient $\alpha^{i+1/2} = \lambda^{i+1/2}\phi^{i+1/2}$ represents a specifically weighted spectral radius, in order to account for highly stretched cells in boundary-layers. The idea is, that each curvilinear coordinate $\xi,\eta,\zeta$ is associated with its own spectral radius, e.g. $\lambda_\xi = |\vec{U}\cdot\vec{S}_\xi| + a|\vec{S}_\xi|$, where $\vec{U}$ is the local velocity vector, $a$ is the local speed of sound, and $\vec{S}_\xi$ is the locally averaged surface normal along $\xi$. The weighting function is then defined according to Radespiel et al. (1990) as

$$\phi_\xi = 1 + \max\left[\left(\frac{\lambda_\eta}{\lambda_\xi}\right)^\omega, \left(\frac{\lambda_\zeta}{\lambda_\xi}\right)^\omega\right],$$

where the exponent $\omega$ controls the weighting. Note, that this scheme is applied only to the RANS equations, whereas the convective fluxes in the turbulence equations are discretized by a simpler first order upwind scheme. All viscous (i.e. diffusive) fluxes are computed using a central discretization, where the first derivatives are averaged to the cell faces. The turbulent source terms are explicitly added, assuming constant values within each volume.

The mean flow equations are integrated in time by an explicit five-stage hybrid Runge–Kutta scheme, which is accelerated by local time stepping, an implicit smoothing of the residuals and a multigrid algorithm (Jameson et al., 1981). According to a detailed analysis of Fassbender (2004), the equations for turbulence quantities are integrated by an implicit scheme on the finest grid level only, where the source terms are linearized in time, which has shown to be a highly efficient and robust approach.

## 3. Results and discussion

The performance of the turbulence models presented are illustrated by computing three transonic flow cases: 2D flow over the RAE2822 airfoil (Cook et al., 1979), 3-D flow past the ONERA M6 wing (Schmitt and Charpin, 1979) and the flow over the DLR-ALVAST wing-body configuration representing a generic transport aircraft model, Burgsmüller and Hoheisel (2000).

Selected results concerning the wall pressure distribution and mean velocity and turbulence fields are displayed and discussed in the following subsections.

### 3.1. RAE2822

The first example is the transonic flow around the RAE2822 airfoil investigated experimentally by Cook et al. (1979). A fairly strong shock is created near the mid chord ($x/c = 0.55$). Two cases, denoted by Case 9 and 10, characterized by $Ma_\infty = 0.73$, $Re_\infty = 6.5\times10^6$ and $Ma_\infty = 0.75$, $Re_\infty = 6.2\times10^6$, respectively, were considered. Both airfoil configurations are at incidence angle of $\alpha = 2.8°$. Important difference between the two flows is a thin, post-shock separation occurring in the case 10. 2D

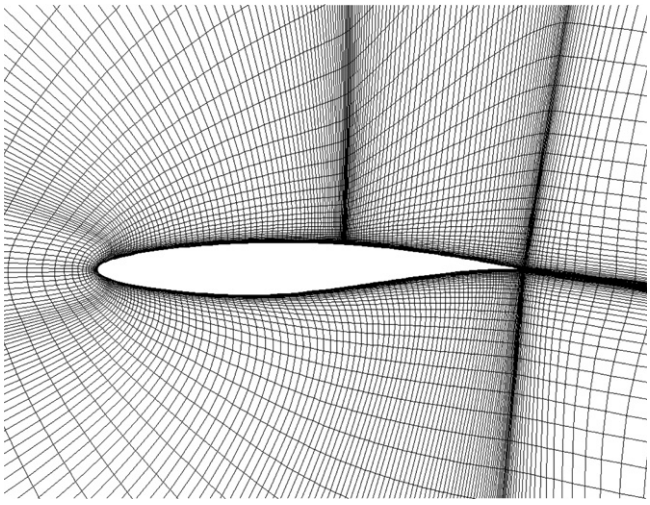

Fig. 5. Blow-up of the C-type grid ($736 \times 176$ cells) used for the computation of the flow past RAE2822 airfoils (every second grid line is shown).

calculations were performed on a C-type grid, Fig. 5. Although there is some doubt regarding the two-dimensionality of the experiments (see e.g. Haase et al., 2006), turbulence models that are capable to predict both cases reasonably well usually perform also well for complex industrial applications in the transonic flow regime. Three grid resolutions were used in the framework of the grid dependence study: coarse (consisting of $184 \times 44$ grid cells), medium ($368 \times 88$ grid cells) and fine ($736 \times 176$ grid cells). It was checked using the SSG/LRR-$\omega$ model that the pressure distributions at the finest and second finest grid level are almost identical (see Fig. 6). Finally, the finest grid, being regarded to be fine enough to ensure grid converged solutions, was adopted for the computations.

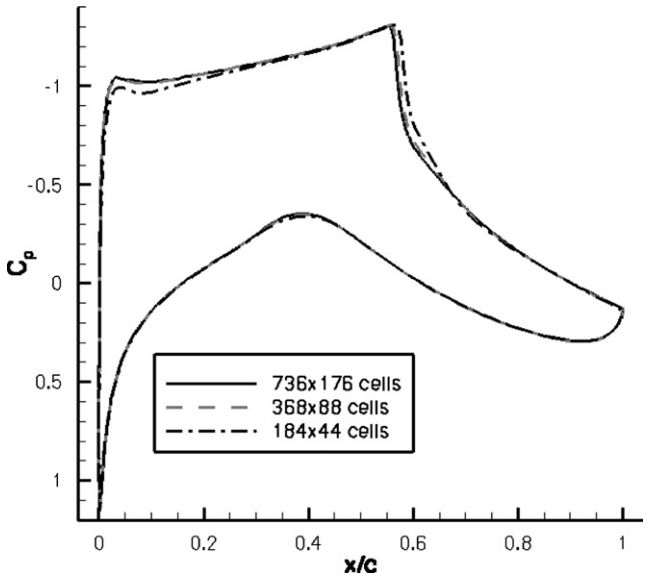


Fig. 6. Effect of grid refinement on pressure distribution for RAE2822 airfoil (case 10) (the SSG/LRR-$\omega$ model was used).

The solution domain is extended to 20 chord lengths in all directions. At the solution domain boundaries the far-field boundary conditions based on the theory of characteristics were applied. Transition to turbulence in the experiment was induced by tripping the flow near the leading edge at $x/c = 0.03$ on both upper and lower surfaces of the airfoil. The computational treatment of this transition location was accounted for by multiplying the entire source term (production, redistribution and dissipation) in the equations governing the Reynolds stresses and dissipation rate by an appropriate step function, providing its zero value in the laminar flow part and a unit value in the fully turbulent flow region. Furthermore, it should be noted that the corrections of the computational results obtained under free-flight conditions with respect to the wind tunnel confinement (experimental conditions) were introduced according to the proposal of Haase et al. (1993).

Fig. 7 shows the comparison of the computed pressure coefficient distribution with available experimental data for both flow configurations considered. Continuous flow acceleration causes considerable pressure rise in the supersonic flow part which ends up in a shock appearance after

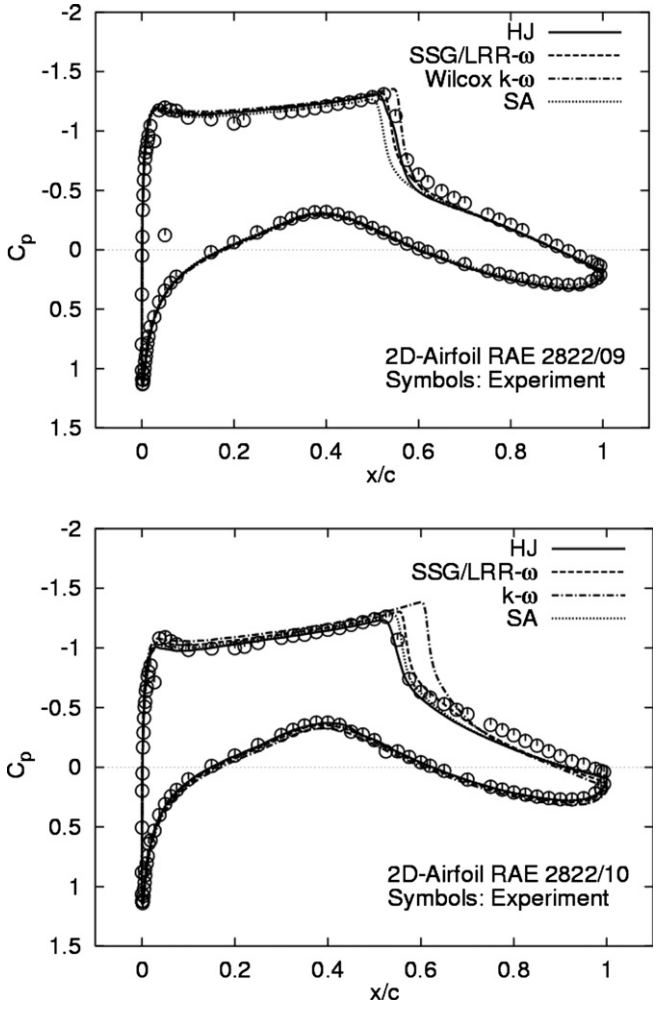


Fig. 7. Pressure coefficient distribution for RAE2822 airfoil: case 9 (upper) and case 10 (lower).

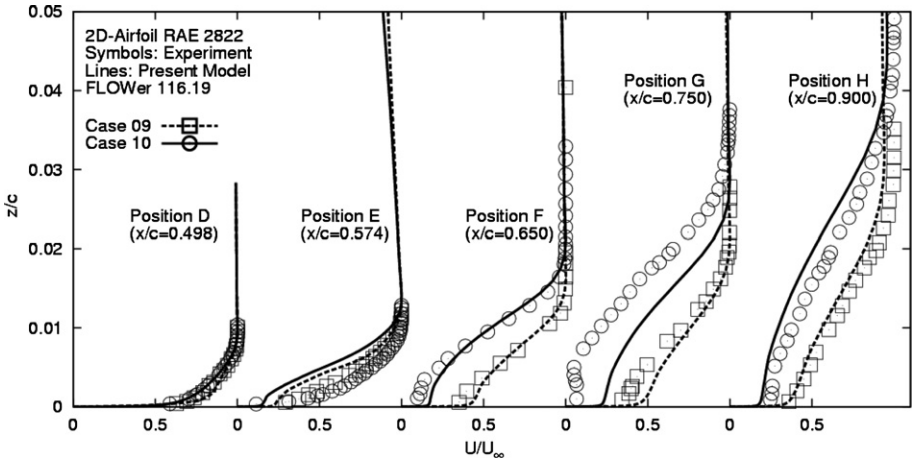


Fig. 8. Mean axial velocity profile evolution in the transonic flow over the upper RAE2822-profile surface for the cases 9 and 10.

reaching an appropriate level. The overall agreement between Reynolds-stress model results and experiment is satisfactory for both configurations in contrast to the results obtained by SA and $k$–$\omega$ models. Whereas the SA model application resulted in a premature shock in the case 9 and correct shock position in the case 10, the $k$–$\omega$ model results indicate a shock positioned too far downstream in the case 10, while returning a correct shock location in the case 9. A slight deviation with respect to the maximum pressure level on the suction side immediately after the leading edge of airfoil (Fig. 7 lower) in the case 10 was obtained by both second-moment closures. The position of the pressure peak coincides with the onset of the turbulent region immediately after transition ($x/c = 0.03$). A fairly crude transition treatment can certainly be the reason for this departure, since the process of the Reynolds-stress component generation pertinent to second-moment closure models is especially sensitive to.

A slight discrepancy with respect to the premature shock location obtained by the HJ model in the case 9 is noticeable in the mean velocity field, Fig. 8. The velocity profile at the location $E$ corresponding to the shock position indicates a somewhat stronger momentum loss. Interestingly, these circumstances don't influence the correct capturing of the flow recovery in the post-shock region. The evolution of the mean velocity field indicates clearly the boundary layer thickening starting at the shock foot, being further enhanced by the adverse pressure gradient effects corresponding to the destabilized wall curvature, i.e. to the continuous cross-section expansion towards the trailing edge of the airfoil. This predicted behaviour is in good agreement with experiment. Both the pre-shock suction pressure and the velocity profile immediately after the shock wave (location F) were captured well in the case 10. However, important discrepancies concerning the post-shock region with respect to the local, low-intensity flow reversal situated around the location G were revealed. It should be recalled here that the experimentally obtained velocity field does not indicate the appearance of flow separation. In some previous computational studies, e.g. Bardina et al. (1997), a slightly higher angle of attack (up to 3.1°) was imposed in order to accommodate the experimental conditions more appropriately. It should also be noted that the present near-wall, Reynolds-stress model due to Hanjalic and Jakirlic has never been tested before in the flows influenced by compressibility. Furthermore, the model version used here does not comprise the two additional terms in the dissipation equation which improve its sensitivity against adverse pressure gradient effects with respect to the intensified normal straining and excessive length-scale increase (see e.g., the works of Jakirlić et al., 2002 and Apsley and Leschziner, 1999). The analysis of the model with respect to the compressibility effects is in progress. The boundary-layer structure is strongly influenced by the sudden pressure increase. Fig. 9 shows the profiles of the normal Reynolds-stress components at two streamwise locations corresponding to the positions D and F, with the shock wave occurring in between. The

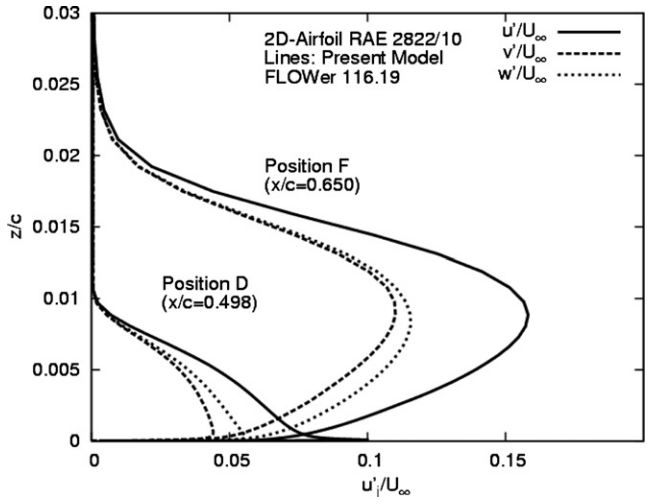


Fig. 9. RMS of the normal components of the Reynolds-stress tensor at two selected locations at the RAE2822/10-profile before and after the shock.

effects of the increasingly varying adverse pressure gradient in the region of shock are demonstrated through the intensive turbulence production (all stress components experienced strong increases) due to strongly enhanced irrotational straining with respect to the rapid flow deceleration.

### 3.2. ONERA M6 wing

Flow over the ONERA M6 semi-span wing (Schmitt and Charpin, 1979) is calculated at $Ma_\infty = 0.84$, $Re_\infty = 11.72 \times 10^6$ and $\alpha = 3.06^\circ$ angle of incidence, Fig. 10. The fully-turbulent calculations were performed at the C–O-type grid comprising $240 \times 64 \times 52$ cells, Fig. 11. This grid was used as the standard structured grid for a cross comparison in the framework of the EU project FLOMANIA (Haase et al., 2006). The grid is sufficiently fine to resolve the immediate wall vicinity. The averaged $y^+$ value of the wall-nearest computational nodes over the entire wing surface corresponds approximately to 1. The solution domain was extended to 7.5 chord lengths in the $x$ and $y$ directions and 9.5 chord lengths in the $z$ direction. Similar as in the previous case, the far-field boundary conditions were applied at the solution domain boundaries. The symmetry boundary conditions were imposed at the $x$–$y$ ($z = 0$) plane, Fig. 11.

The wall pressure contours displayed in Fig. 10 as well as the Mach-number contours (Fig. 12) and the pressure coefficient distribution (Fig. 13) at selected spanwise locations illustrate the region of alternating favourable and adverse pressure gradients causing local acceleration and deceleration within the supersonic part of the flow. The consequence of such flow behaviour is its double-shock-like structure representing a double expansion into the

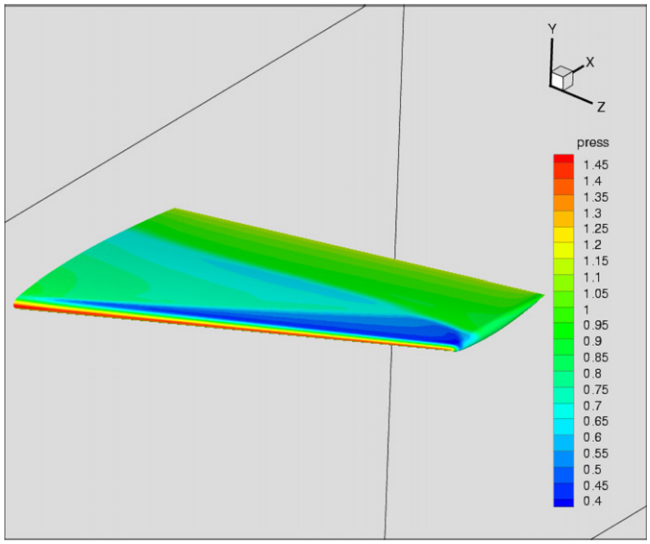


Fig. 10. ONERA M6 wing: wall pressure contours.

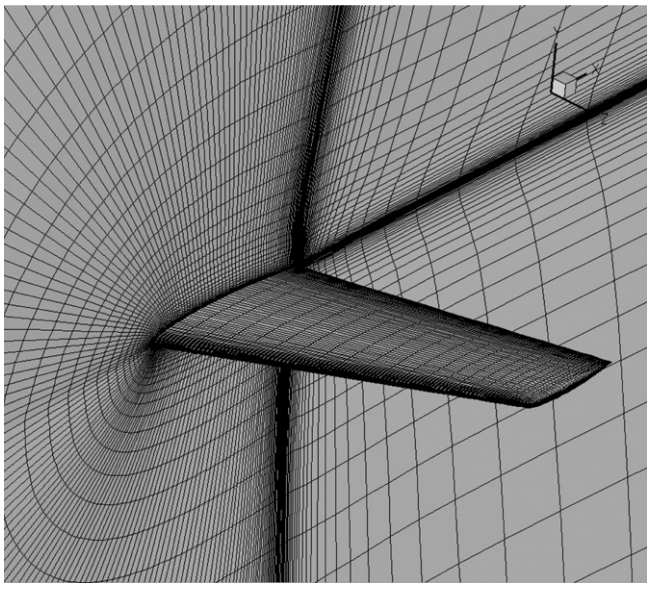

Fig. 11. Computational grid ($240 \times 64 \times 52$ cells) used for the computation of the flow past ONERA M6 wing.

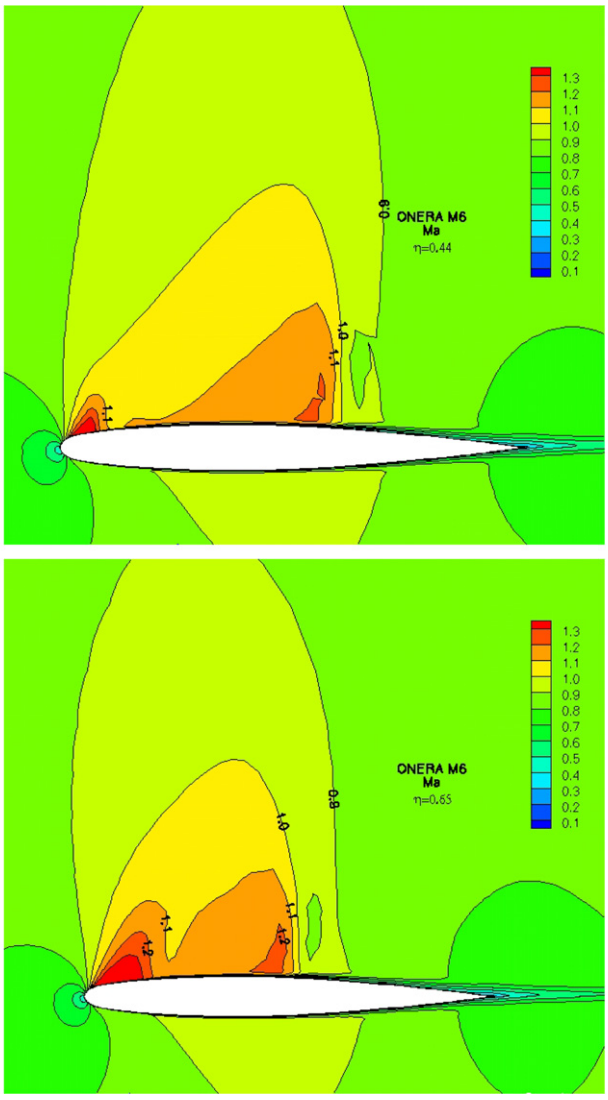


Fig. 12. Mach-number contours in the transonic flow around ONERA M6 wing at 44% and 65% span.

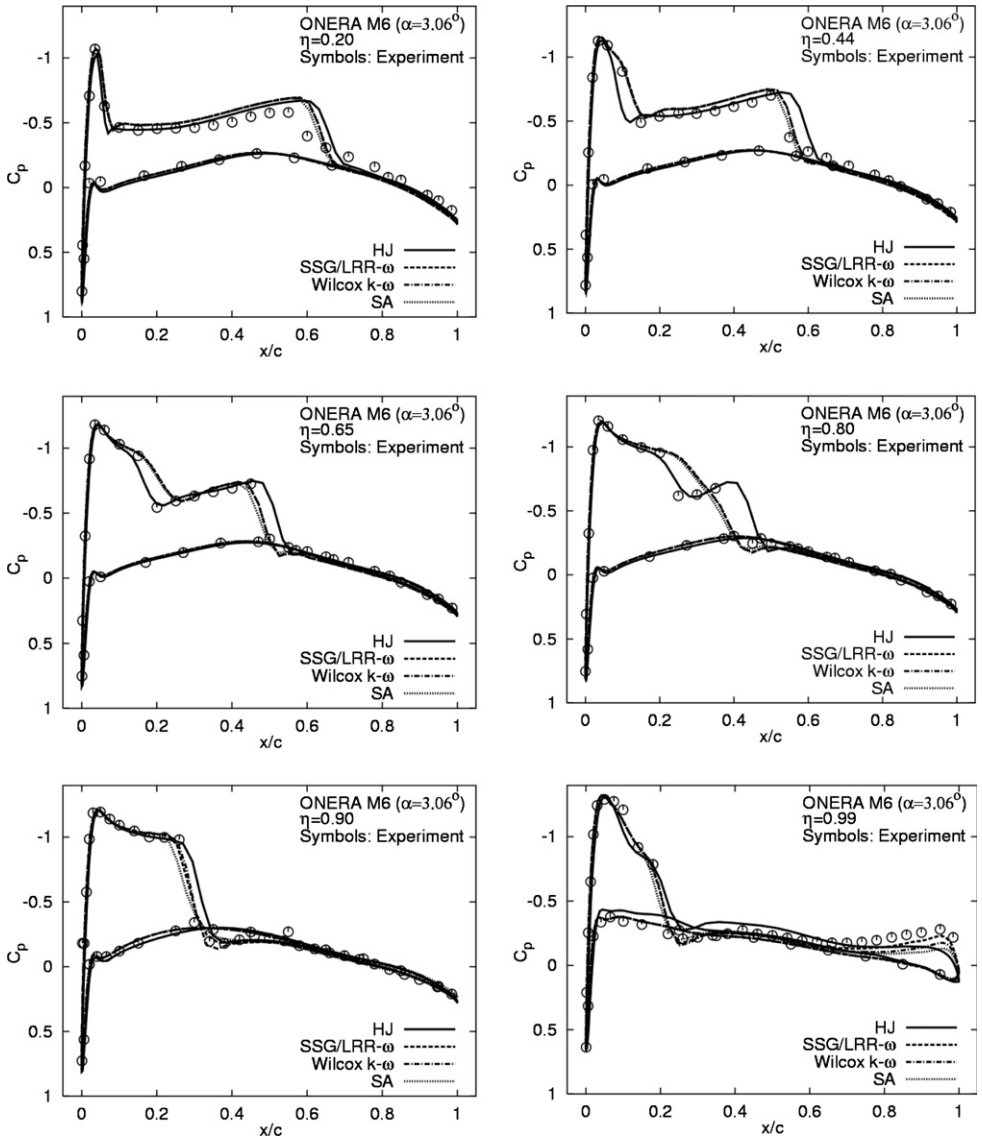


Fig. 13. ONERA M6 wing: pressure coefficient distribution at selected spanwise location.

supersonic regime. The flow experiences a rapid acceleration in the leading edge region of the wing ($x/c = 0.1$–$0.2$) up to $Ma \approx 1.4$, along with the steep rise of the pressure level, Figs. 12 and 13. A prompt deceleration of the flow down to $Ma \approx 1.1$ follows creating consequently a weak shock, whose front propagates within the supersonic region towards the second shock of considerably increased strength. The second shock changes its position depending on the span location. The gradual coalescence of the shocks occurs in the final 15–20% of the wing span in the wing-tip region, Fig. 13. The varying positions of both shocks with respect to the spanwise location as well as the wall pressure magnitude over the entire wing surface are reasonably well captured by all models. The pressure coefficient distribution illustrates the equality of the wall pressure values at both wing surfaces over the whole wing span corresponding to the second half of the chord. The only exception is the last spanwise position situated directly at the wing tip, $\eta = 0.99$. Here, the influence of the tip vortex created by the flow from the lower wing surface towards the upper wing surface around the tip is clearly visible in the pressure distribution. This feature is reasonably well captured by the present Reynolds-stress transport models. All model predictions are of comparable quality, the only significant difference is documented at the location corresponding to 80% of the span. Here, the HJ model returned the double-shock structure in correct agreement with experimental results, whereas the other models applied predicted a premature coalescence of two shock fronts. While the position and strength of the first shock at the spanwise positions $\eta = 0.44$, 0.65 and 0.80 obtained by applying the HJ model agree well with the experimental data, the predicted position of the second shock exhibits a certain delay compared to the measurements and other model results. The results obtained by LRR/SSG and eddy-viscosity models (positions $\eta = 0.44$ and 0.65) display correct onset of the first

shock. However, the course of its front (milder slope), whose foot is shifted downstream, indicates the pressure relaxation of a somewhat lower intensity compared to a steeper pressure gradient obtained by the HJ model. The final outcome of such a situation reflects a gradual shortening of the region between two shocks (characterized by a mild pressure increase) until their premature merging at $\eta = 0.80$.

### 3.3. DLR-ALVAST

The DLR-ALVAST is a generic transport aircraft model that can be equipped with turbine-driven engine simulators (Kiock, 1996). It has been used, e.g. in the EU-project ENIFAIR, for studying engine interference effects (Burgsmüller and Hoheisel, 2000). In the present work numerical simulations have been performed for the clean wing configuration (Fig. 14) at a free stream Mach number of $Ma_\infty = 0.75$ and a Reynolds number of $Re = 4.3 \times 10^6$ based on the mean chord length. The incidence has been varied to achieve a lift coefficient of $C_L = 0.5$, which is the design point.

The computations with the SSG/LRR-$\omega$ model have been carried out on a grid consisting of $4.1 \times 10^6$ cells (this grid was adopted from the study of Fassbender, 2004). Particular care has been taken in the grid generation process, focussing especially on properly resolving the boundary-layer over the entire aircraft surface (with 20–24 grid cells accommodated in the normal-to-the-wall direction). The near-wall grid lines have a wall distance well below $y_1^+ = 1$ over the entire geometry, except a small portion at the fuselage tail. The artificial dissipation coefficients have been set to $k^{(2)} = 1/2$ for first-order accuracy at shocks and to $k^{(4)} = 1/32$ for second-order in regions where the solution is smooth (see Section 2.2). The relatively high value of the latter coefficient has been necessary in order to damp oscillations that are generated by a separation zone at the wing-body junction. The settings of these coefficients influence mainly the strength of the shock (not the position) with respect to the pressure difference at the shock itself (immediately before and after the shock) in the streamwise direction (the higher the values of the dissipation coefficients, the weaker, i.e. the more smeared out, the shock), as it was investigated by Kroll and Jain (1987). Nevertheless a rather low value of the Martinelli coefficient (Martinelli and Jameson, 1988) of $\zeta = 0.3$ could have been used, avoiding excessive artificial dissipation in highly stretched cells. The computations with the HJ model experienced some stability problems, whose debugging is in progress. On the other hand, the flow structure over the DLR-ALVAST wing is characterized by a single shock similar to the RAE2822 cases. Accordingly, it was not expected that the HJ model results would have been substantially different compared to those obtained with the LRR/SSG-$\omega$ model. In the following only the latter results will be presented.

Fig. 15 show the pressure distributions in two span-wise wing sections obtained with the SSG/LRR-$\omega$ Second-Moment Closure in comparison with experimental data from the EU-project ENIFAIR in the ONERA S1MA

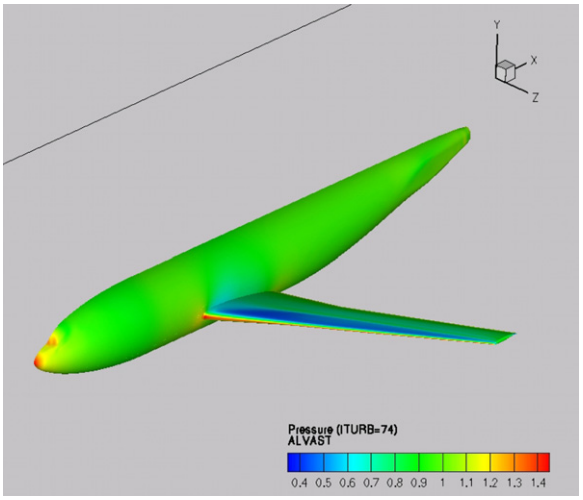


Fig. 14. DLR-ALVAST wing-body configuration: wall pressure contours.

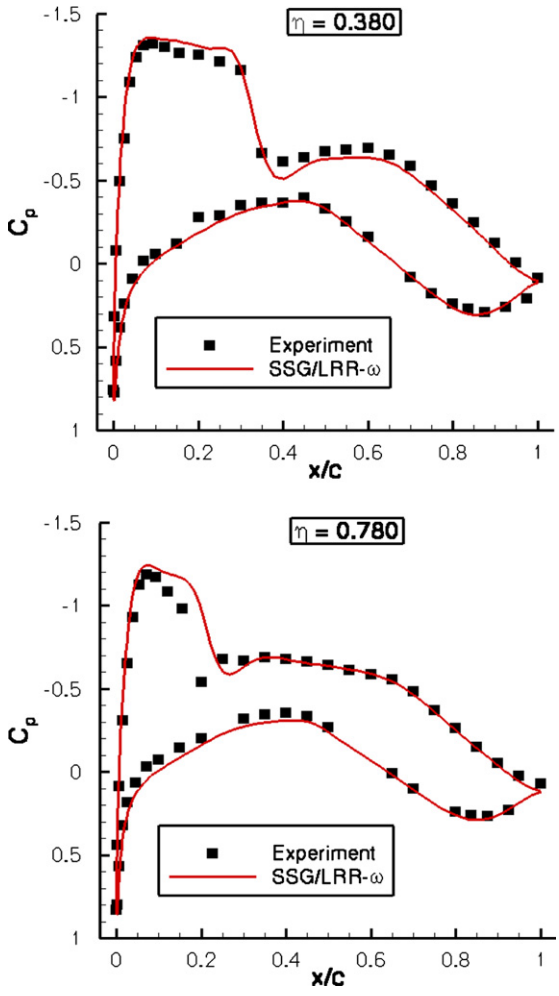


Fig. 15. DLR-ALVAST generic aircraft: experimental and numerical pressure distribution at 38% and 78% span.

wind tunnel (Burgsmüller and Hoheisel, 2000). While the overall agreement is fairly good, some deviations occur with respect to the shock position. It is observed that in the inboard part of the wing the shock is predicted upstream of the measured position, while outboard it is predicted downstream of the measured position towards the wing tip. These deviations can to some extent also be attributed to the fact that the aircraft model (made of plastics) heated up, hence deformed during the experiments (see e.g., the work of Hoheisel, 1999).

### 3.4. Numerical issues

The following statements can be made with respect to the numerical robustness of the Reynolds-stress models. The SSG/LRR-$\omega$ model requires about 100% more CPU time per iteration compared to the Wilcox $k$–$\omega$ model. Generally, the number of iterations needed depends on the flow problem and is not necessarily higher when using a Reynolds stress model. In the case of the ONERA M6 wing 1500 iterations have been used with the Wilcox $k$–$\omega$ model and 2500 with the SSG/LRR-$\omega$ model. Hereby, the first 700 iterations have been performed on coarse grids (full multigrid). The iteration number for the HJ model is somewhat higher, but only with respect to the generation of the initial fields of the turbulent quantities in the immediate wall vicinity. These circumstances relate to the initial field (the HJ model computations started from the LRR/SSG model results) adjustment to the HJ model equations.

## 4. Conclusions

The performance of a near-wall, Reynolds-stress turbulence model accounting separately for the viscous effects and the effects of Reynolds-stress and dissipation anisotropy are investigated under the transonic flow conditions characterized by the shock formation and strong shock/boundary-layer interaction in several two-dimensional and three-dimensional flow configurations. The overall agreement with the available experimental data for the surface pressure distribution with respect to the shock position is satisfactory in all flow configurations computed. A double-shock-like structure of the flow over the ONERA-M6 wing was captured, in good agreement with the experimental findings. Important departures are revealed concerning the shock-induced separation at the RAE2822/10 airfoil. Despite a correctly predicted shock position, the departure from the experimentally obtained post-shock pressure level caused the flow to remain attached. Further analysis of these phenomena is necessary, especially with respect to the specific model features that require consideration concerning the compressibility effects and the conditions of strong property variation. Computations were also performed by using another near-wall, Reynolds-stress transport closure with constant model coefficients (LRR/SSG-$\omega$) as well as with two widely used eddy-viscosity-based transport model schemes, one-equation $v_t$-transport model (Spalart and Allmaras, 1994) and the $k$–$\omega$ due to Wilcox (1988). With the exception of the premature shock waves coalescence in the ONERA-M6 case, the LRR/SSG-$\omega$ model predictions follow reasonably the HJ model results with respect to the pressure distribution in all configurations considered, despite its inferiority in capturing the near-wall Reynolds-stress anisotropy.

## Acknowledgements

The present work was performed in the framework of the German project MEGADESIGN dealing with the aerodynamic simulation and optimization in the aircraft design. The financial support of the German Ministry for Economy and Technology (BMWi) through the grant 20A0302K for R. Jester-Zürker is gratefully acknowledged.

## References

Apsley, D.D., Leschziner, M.A., 1999. Advanced turbulence modelling of separated flow in a diffuser. Flow, Turbulence and Combustion 63, 81–112.

Baldwin, B.S., Lomax, H., 1978. Thin layer approximation and algebraic model for separated turbulent flows. AIAA Paper 78-0257.

Barakos, G., Drikakis, D., 2000. Numerical simulation of transonic buffet using various turbulence closures. International Journal of Heat and Fluid Flow 21, 620–626.

Bardina, J.E., Huang, P.G., Coakley, T.J., 1997. Turbulence modelling validation, testing and development. NASA Technical Memorandum 110446.

Batten, P., Craft, T.J., Leschziner, M.A., Loyau, H., 1999. Reynolds-stress-transport modelling for compressible aerodynamics application. AIAA Journal 37 (7), 785–797.

Burgsmüller, W., Hoheisel, H., 2000. ENIFAIR – EU research into engine integration on future transport aircraft. Air and Space Europe 2 (2), 81–85.

Cebeci, T., 1999. An Engineering Approach to the Calculation of Aerodynamic Flows. Horizons Publishing, Springer.

Cebeci, T., Smith, A.M.O., 1974. Analysis of turbulent boundary layers. Series in Applied Mathematics and Mechanics XV. Academic Press, London.

Cook, P.H., McDonald, M.A., Firmin, M.C.P., 1979. Aerofoil RAE 2822 – Pressure distributions, and boundary layer and wake measurements: experimental data base for computer program assessment. Report of the Fluid Dynamics Panel Working Group 04, AGARD AR 138.

Eisfeld, B., 2006. Numerical simulation of aerodynamic problems with a Reynolds stress turbulence model. In: Rath, H.-J. et al. (Eds.), Notes on Numerical Fluid Mechanics, vol. 92. Springer, pp. 413–421.

Eisfeld, B., Brodersen, O., 2005. Advanced turbulence modelling and stress analysis for the DLR-F6 configuration. AIAA Paper 2005-4727.

Fassbender, J.K., 2004. Improved Robustness for Numerical Simulation of Turbulent Flows around Civil Transport Aircraft at Flight Reynolds Numbers. DLR-Forschungsbericht 2003-09.

Gerolymos, G.A., Vallet, I., 2002. Wall-normal-free near-wall Reynolds-stress model for 3-D turbomachinery flows. AIAA Journal 40 (2), 199–208.

Gibson, M.M., Launder, B.E., 1978. Grounds effects on pressure fluctuations in the atmospheric boundary layer. Journal of Fluid Mechanics 86, 491–511.

Haase, W., Brandsma, F., Elsholz, E., Leschziner, M.A., Schwamborn, D., 1993. EUROVAL – A European Initiative on Validation CFD CodesNotes on Numerical Fluid Mechanics, vol. 42. Vieweg Verlag, Braunschweig.

Haase, W., Chaput, E., Elsholz, E., Leschziner, M.A., Müller, U., 1997. ECARP – European Computational Aerodynamics Research Project on Validation of CFD Codes and Assessment of Turbulence ModelsNotes on Numerical Fluid Mechanics, vol. 58. Vieweg Verlag, Braunschweig/Wiesbaden.

Haase, W., Aupoix, B., Bunge, U., Schwamborn, D., 2006. FLOMANIA – A European Initiative on Flow Physics ModellingNotes on Numerical Fluid Mechanics and Multidisciplinary Design, vol. 94. Springer.

Hanjalic, K., Jakirlic, S., 1998. Contribution towards the second-moment closure modelling of separating turbulent flows. Computers and Fluids 22 (2), 137–156.

Hanjalić, K., Jakirlić, S., 2002. Second-moment turbulence closure modelling. In: Launder, B.E., Sandham, N.H. (Eds.), Closure Strategies for Turbulent and Transitional Flows. Cambridge University Press, Cambridge, UK, pp. 47–101.

Hoheisel, H., 1999. Data evaluation of the ENIFAIR high speed tests. DLR-Report, DLR-IB 129-99/11.

Jakirlić, S., 2004. DNS-based scrutiny of RANS-approaches and their potential for predicting turbulent flows. Habilitation Thesis, Darmstadt University of Technology.

Jakirlić, S., Hanjalić, K., 1995. A second-moment closure for non-equilibrium and separating high- and low-Re-number flows. In: Proc. 10th Symposium on Turbulent Shear Flows. The Pennsylvania State University, USA, pp. 14–16. August.

Jakirlić, S., Hadzić, I., Djugum, A., Tropea, C., 2002. Boundary-layer separation computed by second-moment closure models. In: Wagner, S. et al. (Eds.), Notes on Numerical Fluid Mechanics, vol. 77. Springer, pp. 215–222.

Jameson, A., Schmidt, W., Turkel, E., 1981. Numerical solutions of the Euler equations by finite volume methods using Runge–Kutta time-stepping schemes. AIAA Paper 81-1259.

Johnson, D.A., King, L.S., 1985. A mathematical simple turbulence closure model for attached and separated turbulent boundary layers. AIAA Journal 23, 1684–1692.

Kiock, R., 1996. The ALVAST Model of DLR. DLR-Institutsbericht 129-96/22.

Kroll, N., Jain, R.K., 1987. Solution of Two-Dimensional Euler Equations – Experience with a Finite Volume Code. DFVLR-Forschungsbericht, DFVLR-FB 87-41.

Kroll, N., Radespiel, R., Rossow, C.-C., 1995. Accurate and Efficient Flow Solvers for 3D Applications on Structured Meshes. In: Special Course on Parallel Computing in CFD. AGARD-Report R-807 (Chapter 4).

Kroll, N., Rossow, C.C., Becker, K., Thiele, F., 2000. The MEGAFLOW project. Aerospace Science and Technology 4, 223–237.

Kroll, N., Rossow, C.C., Schwamborn, D., Becker, K., Heller, G., 2002. MEGAFLOW – A numerical simulation tool for transport aircraft design. ICAS Congress 2002, Paper No. 1.10.5.

Launder, B.E., Reece, G.J., Rodi, W., 1975. Progress in the development of Reynolds-stress turbulence closure. Journal of Fluid Mechanics 68, 537–566.

Le, H., Moin, P., Kim, J., 1997. Direct numerical simulation of turbulent flow over a backward-facing step. Journal of Fluid Mechanics 330, 349–374.

Leschziner, M.A., Drikakis, D., 2002. Turbulence modelling and turbulent-flow computation in aeronautics. The Aeronautic Journal (July), 349–383.

Leschziner, M.A., Lien, F.-S., 1997. Computational Modelling of Turbulent Aerodynamic Flows within the ECARP Programme using Anisotropy-Resolving ClosuresNotes on Numerical Fluid Mechanics, vol. 58. Vieweg Verlag, Braunschweig/Wiesbaden, pp. 279–290.

Leschziner, M.A., Batten, P., Loyau, H., 2000. Modelling shock-affected near-wall flows with anisotropy-resolving turbulence closures. International Journal of Heat and Fluid Flow 21, 239–251.

Martinelli, L., Jameson, A., 1988. Validation of a multigrid method for the Reynolds averaged equations. AIAA Paper 88-0414.

Menter, F.R., 1994. Two equation eddy viscosity turbulence models for engineering applications. AIAA Journal 32, 1598–1605.

Moser, R.D., Kim, J., Mansour, N.N., 1999. Direct numerical simulation of turbulent channel flow up to $Re_\theta = 590$. Physics of Fluids 11 (4), 943–945.

Radespiel, R., Rossow, C., Swanson, R., 1990. Efficient cell-vertex multigrid scheme for the three-dimensional Navier–Stokes equations. AIAA Journal 28 (8), 1464–1472.

Schmitt, V., Charpin, F., 1979. Pressure distributions on the ONERA-M6-wing at transonic mach numbers: Experimental data base for computer program assessment. Report of the Fluid Dynamics Panel Working Group 04, AGARD AR 138.

Spalart, P.R., Allmaras, S.R., 1994. A one-equation turbulence model for aerodynamic flows. La Recherche Aérospatiale 1, 5–21.

Speziale, C.G., Sarkar, S., Gatski, T.B., 1991. Modelling the pressure–strain correlation of turbulence: an invariant dynamical systems approach. Journal of Fluid Mechanics 227, 245–272.

Wilcox, D.C., 1988. Reassessment of the scale-determining equation for advanced turbulence models. AIAA Journal 26, 1299–1310.

Wilcox, D.C., 1998. Turbulence modelling for CFD, second ed. DCW Industries, La Canada, USA.